Modelling and Simulation in Materials Science and Engineering

PAPER

A comparison of different continuum approaches in modeling mixed-type dislocations in Al

To cite this article: Shuozhi Xu *et al* 2019 *Modelling Simul. Mater. Sci. Eng.* **27** 074004

IOP Publishing Modelling and Simulation in Materials Science and Engineering

Modelling Simul. Mater. Sci. Eng. **27** (2019) 074004 (21pp) https://doi.org/10.1088/1361-651X/ab2d16

A comparison of different continuum approaches in modeling mixed-type dislocations in Al

Shuozhi Xu[1], Lauren Smith[2], Jaber R Mianroodi[3,4], Abigail Hunter[5], Bob Svendsen[3,4] and Irene J Beyerlein[1,2,6]

[1] California NanoSystems Institute, University of California, Santa Barbara, CA 93106-6105, United States of America
[2] Materials Department, University of California, Santa Barbara, CA 93106-5050, United States of America
[3] Microstructure Physics and Alloy Design, Max-Planck-Institut für Eisenforschung GmbH, Düsseldorf, D-40237, Germany
[4] Material Mechanics, RWTH Aachen, Aachen, D-54062, Germany
[5] X Computational Physics Division, Los Alamos National Laboratory, Los Alamos, NM 87545, United States of America
[6] Department of Mechanical Engineering, University of California, Santa Barbara, CA 93106-5070, United States of America

E-mail: shuozhixu@ucsb.edu

Received 21 February 2019, revised 21 June 2019
Accepted for publication 26 June 2019
Published 17 July 2019

Abstract

Mixed-type dislocations are prevalent in metals and play an important role in their plastic deformation. Key characteristics of mixed-type dislocations cannot simply be extrapolated from those of dislocations with pure edge or pure screw characters. However, mixed-type dislocations traditionally received disproportionately less attention in the modeling and simulation community. In this work, we explore core structures of mixed-type dislocations in Al using three continuum approaches, namely, the phase-field dislocation dynamics (PFDD) method, the atomistic phase-field microelasticity (APFM) method, and the concurrent atomistic-continuum (CAC) method. Results are benchmarked against molecular statics. We advance the PFDD and APFM methods in several aspects such that they can better describe the dislocation core structure. In particular, in these two approaches, the gradient energy coefficients for mixed-type dislocations are determined based on those for pure-type ones using a trigonometric interpolation scheme, which is shown to provide better prediction than a linear interpolation scheme. The dependence of the in-slip-plane spatial numerical resolution in PFDD and CAC is also quantified.

Keywords: mixed-type dislocations, face-centered cubic metals, continuum modeling

(Some figures may appear in colour only in the online journal)

1. Introduction

Dislocations are the main carriers of plastic deformation in metals and are responsible for their characteristic malleability [1]. From a continuum viewpoint, the geometry of a dislocation can be described by two independent variables, line direction $\boldsymbol{l}$ and Burgers vector $\boldsymbol{b}$, the latter of which describes the magnitude and direction of the net lattice displacement. The angle θ between $\boldsymbol{l}$ and $\boldsymbol{b}$ is termed the character angle of a dislocation and ranges from 0° ($\boldsymbol{l}\|\boldsymbol{b}$) for a screw dislocation to 90° ($\boldsymbol{l}\perp\boldsymbol{b}$) for an edge dislocation. Because of their simple and representative geometric configurations, most modeling studies in dislocations have been devoted to those of pure edge/screw type [2].

While much is known about pure-type dislocations, the physics of mixed-type dislocations, which possess character angles θ between 0° and 90°, remains relatively lightly explored computationally. Mixed-type dislocations are prevalent in metals because for a given $\boldsymbol{b}$ in the lattice, θ can have any value between the two extremes if $\boldsymbol{l}$ is infinitesimally varied. To date descriptions of dislocation cores have been best provided by atomic-scale simulations, which find that key characteristics of mixed-type dislocations cannot simply be extrapolated from those of pure-type ones [3–9]. Moreover, atomistic simulations are limited to nano/submicron length scale even with dedicated high-performance computing resources [10]. Thus, to understand plastic deformation of bulk materials, continuum modeling of dislocation core structures is desirable [11].

One type of continuum dislocation models is energy-based, in which dislocations are assumed to evolve such that the free energy of the dislocated system approaches a local minimum [12]. An example is the phase-field (PF) dislocation model, the first of which was proposed by Khachaturyan [13] and Wang *et al* [14] based on gradient thermodynamics of phase transformations, and was termed phase-field microelasticity (PFM). Since then, the PFM method was advanced extensively. For dislocations in face-centered cubic (FCC) crystals, for example, Shen and Wang [15] reformulated the gradient energy density to allow for correct core–core interactions among perfect dislocations on the same slip plane. The author of [16] related the crystalline energy to the generalized stacking fault energy (GSFE). Mianroodi and Svendsen [17] furthered the gradient energy coefficients with the Shockley partial dislocation cores obtained in atomistic simulations. In 2014, Shen *et al* [18] proposed the microscopic phase-field model in which all order parameter evolution is confined to the slip planes and the gradient energy is removed from the system energy. More recently, Zheng *et al* [19] modified the crystalline energy to fully account for the reactions between dislocations gliding in intersecting slip planes, while also neglecting the gradient energy.

Besides PFM, another branch of the PF dislocation model is based on the phase-field theory of dislocation dynamics proposed by Koslowski *et al* [20], in which the gradient energy was not included in the system energy. For the model to be analytically tractable, Koslowski *et al* [20] did not use numerical grids in solving the energy functional. Later, Koslowski and Ortiz [21] extended their earlier work [20] to a multi-phase field model, in which numerical grids were employed. In 2011, the same model was extended to 3D and termed as phase-field dislocation dynamics (PFDD) [22–25]. Since then, PFDD has been employed to study a series of dislocation-mediated problems in multiple crystalline materials.

We refer the reader to the review article of Beyerlein and Hunter [26] for further background information on PFDD. Mianroodi *et al* [27] showed that the previous PFDD variant was a model of generalized Peierls–Nabarro (GPN) type. More specifically, it was mathematically different from, but physically the same as, for example the GPN model of Xiang *et al* [28]. In the current work, the PFDD energy model is extended by inclusion of the gradient energy analogous to that in PFM. The resulting 'gradient' PFDD model is mathematically different from but physically the same as PFM, and so APFM. In what follows, unless stated otherwise, the newly extended PFDD model will be referred to as 'PFDD' for brevity. A distinction will be made when the new model is compared with the previous one.

In this work, we explore core structures of mixed-type dislocations in FCC Al using three continuum dislocation models, including PFDD, APFM, and the concurrent atomistic-continuum (CAC) method [29, 30]. Among all PF dislocation models, PFDD and APFM are chosen because they are atomistically-informed, and we will validate them in this paper by benchmarking their results against molecular statics (MS). Note that straight mixed-type dislocations have been studied by CAC in Al and Cu [30], but not by PFDD or APFM. Nevertheless, there is no theoretical challenge in applying the two PF-based methods to straight mixed-type dislocations since they have been employed to simulate curved dislocations [31, 32] and dislocation loops [17, 24]. In particular, we have advanced both PFDD and APFM in several aspects, enabling better representation of mixed-type dislocations compared with previous work.

Before reviewing the formulations in each method, we present the notation we will use. 3D Euclidean vectors are represented by lower-case boldfaced, italicized characters $\boldsymbol{a}$, $\boldsymbol{b}$,…. Cartesian basis vectors are represented by $\boldsymbol{i}_x$, $\boldsymbol{i}_y$, $\boldsymbol{i}_z$. Second-rank tensors are represented by upper-case boldfaced, italicized characters $\boldsymbol{A}$, $\boldsymbol{B}$,…, with $\boldsymbol{I}$ being the second-rank identity matrix. $\mathcal{A} \cdot \mathcal{B} = A_{ij\ldots}B_{ij\ldots}$ is the scalar product of two tensors of arbitrary order. Fourth-rank Euclidean tensors A, B,… are denoted by upper-case slanted sans-serif characters. $(\boldsymbol{a} \otimes \boldsymbol{b})\boldsymbol{c} = (\boldsymbol{b} \cdot \boldsymbol{c})\boldsymbol{a}$ defines the dyadic product $\boldsymbol{a} \otimes \boldsymbol{b}$ of $\boldsymbol{a}$ and $\boldsymbol{b}$, $\boldsymbol{A}^{\mathrm{T}}\boldsymbol{b} \cdot \boldsymbol{c} = \boldsymbol{b} \cdot \boldsymbol{A}\boldsymbol{c}$ defines the transpose $\boldsymbol{A}^{\mathrm{T}}$ of $\boldsymbol{A}$, and $\boldsymbol{A}^{\mathrm{T}}\boldsymbol{B} \cdot \boldsymbol{C} = \boldsymbol{B} \cdot \boldsymbol{A}\boldsymbol{C}$ defines the transpose A^{T} of A. Additional notations will be introduced as needed in what follows.

2. Methodology

In this section, we provide theoretical background on the PF-based dislocation model and the CAC method. Hereinafter b and b_{p}, respectively, denote the magnitude of the Burgers vector of a full dislocation $\boldsymbol{b} = (a_0/2)\langle 110\rangle$ and a Shockley partial dislocation $\boldsymbol{b}_{\mathrm{p}} = (a_0/6)\langle 112\rangle$, where a_0 is the lattice parameter.

2.1. Phase-field-based dislocation model

Let $\boldsymbol{u}$ represent the displacement field, $\boldsymbol{H} = \nabla\boldsymbol{u}$ the distortion field, $\boldsymbol{E} = (\boldsymbol{H} + \boldsymbol{H}^{\mathrm{T}})/2$ the strain field, C_{E} the elastic stiffness tensor, and γ_{gsf} the GSFE per unit area. In a PF-based dislocation model, an order parameter ϕ_α represents the state of slip for the αth slip system, with $\phi_\alpha = 0$ and 1 corresponding to the unslipped and slipped states, respectively. In an FCC lattice, a full dislocation within a $\{111\}$ plane is usually dissociated into two Shockley partial dislocations bounding an intrinsic stacking fault (ISF). Thus, a dislocation in the αth slip system in Al spans the region for which $0 < \phi_\alpha < 1$.

For single-element FCC materials, the total free energy density ψ is the sum of the elastic energy density ψ_{ela}, the GSFE density ψ_{gsf}, and the gradient energy density ψ_{gra} [13, 14], i.e.,

$$\psi(\boldsymbol{E},\,\boldsymbol{\phi},\,\nabla\boldsymbol{\phi}) = \psi_{\text{ela}}(\boldsymbol{E},\,\boldsymbol{\phi}) + \psi_{\text{gsf}}(\boldsymbol{\phi}) + \psi_{\text{gra}}(\nabla\boldsymbol{\phi}). \tag{1}$$

In particular,

$$\psi_{\text{ela}}(\boldsymbol{E},\,\boldsymbol{\phi}) = \tfrac{1}{2}(\boldsymbol{E} - \boldsymbol{E}_{\text{R}}(\boldsymbol{\phi})) \cdot \boldsymbol{C}_{\text{E}}(\boldsymbol{E} - \boldsymbol{E}_{\text{R}}(\boldsymbol{\phi})) \tag{2}$$

$$\psi_{\text{gsf}}(\boldsymbol{\phi}) = \frac{\gamma_{\text{gsf}}(\boldsymbol{\phi})}{l_{\text{gsf}}} \tag{3}$$

$$\psi_{\text{gra}}(\nabla\boldsymbol{\phi}) = \sum_{\alpha,\beta=1}^{n} \eta_{\text{g0}}^{\alpha\beta}\, \nabla\phi_\alpha \cdot \boldsymbol{N}_{\alpha\beta}\nabla\phi_\beta, \tag{4}$$

where n is the total number of order parameters, $\boldsymbol{E}_{\text{R}} = (\boldsymbol{H}_{\text{R}} + \boldsymbol{H}_{\text{R}}^{\text{T}})/2$ is the residual strain, l_{gsf} is the interplanar spacing between two adjacent slip planes based on which γ_{gsf} is calculated, and $\eta_{\text{g0}}^{\alpha\beta}$ are gradient energy coefficient, and

$$\boldsymbol{H}_{\text{R}}(\boldsymbol{\phi}) = \sum_{\alpha=1}^{n} \frac{b_\alpha\phi_\alpha}{d_\alpha}\, \boldsymbol{s}_\alpha \otimes \boldsymbol{n}_\alpha \tag{5}$$

$$\boldsymbol{N}_{\alpha\beta} = \frac{\boldsymbol{b}_\alpha \cdot \boldsymbol{b}_\beta}{d_\alpha d_\beta}[(\boldsymbol{n}_\alpha \cdot \boldsymbol{n}_\beta)\boldsymbol{I} - \boldsymbol{n}_\beta \otimes \boldsymbol{n}_\alpha], \tag{6}$$

where $\boldsymbol{s}_\alpha$ is the slip direction, $\boldsymbol{n}_\alpha$ is the slip plane unit normal, $\boldsymbol{b}_\alpha = b_\alpha\boldsymbol{s}_\alpha$ is the slip vector, and d_α is the interplanar spacing between two adjacent slip planes, of the αth order parameter. In the current work of a single slip plane in FCC crystals, $d_\alpha = d_\beta = l_{\text{gsf}} = d_{111} = a_0/\sqrt{3}$, where d_{111} is the interplanar distance between two $\{111\}$ planes. ψ_{gsf} represents the density of energy stored in stacking faults (e.g. ISF) and partial dislocation (e.g. Shockley partial) cores, while ψ_{gra} the density of energy stored in the latter only.

It follows that the time-dependent Ginzburg–Landau (TDGL) equation is employed to recursively minimize the system free energy with respect to each ϕ_α, i.e.,

$$\dot{\phi}_\alpha = m_0[\nabla \cdot \partial_{\nabla\phi_\alpha}\psi_{\text{gra}} - \partial_{\phi_\alpha}(\psi_{\text{ela}} + \psi_{\text{gsf}})], \tag{7}$$

where the superposed dot denotes the time derivative and the Ginzburg–Landau coefficient m_0 is non-negative and assumed constant here. Once all ϕ_α are determined, the disregistry field ζ_β along the β direction is calculated by

$$\zeta_\beta = \sum_{\alpha=1}^{n_{\text{sp}}} \phi_\alpha\, \boldsymbol{b}_\alpha \cdot \boldsymbol{s}_\beta, \tag{8}$$

where n_{sp} is the total number of order parameters on the slip plane within which the αth order parameter and β direction lie. In this paper, $\beta = 1$ and $\beta = 2$ represent the directions along and normal to the full dislocation Burgers vector, respectively.

As discussed in our previous work [27, 33], different modeling choices are made in PFDD and APFM. In what follows, subscripts or superscripts P and A are used to denote quantities in PFDD and APFM, respectively. In PFDD, the slip vector $\boldsymbol{b}_\alpha^{\text{P}} = \boldsymbol{b}$ is along a $\langle 110\rangle$ direction, and three order parameters are used for each slip plane in an FCC lattice. Thus, in PFDD, for a single slip plane, $n_{\text{P}} = 3$ and there are nine gradient energy coefficients $\eta_{\text{P}}^{\alpha\beta}$ in equation (4). In APFM, the slip vectors $\boldsymbol{b}_1^{\text{A}} = \boldsymbol{b}$ and $\boldsymbol{b}_2^{\text{A}} = (a_0/2)\langle 112\rangle$ are perpendicular to each other, i.e. $\boldsymbol{N}_{12} = \boldsymbol{N}_{21} = \boldsymbol{0}$ in equation (4). Thus, in APFM, for a single slip plane, $n_{\text{A}} = 2$ and there are two non-trivial coefficients, η_{A}^{11} and η_{A}^{22}.

We remark that the form of the gradient energy density ψ_{gra}, including the determination of the coefficients $\eta_{\text{g0}}^{\alpha\beta}$, is the focus of on-going research and model development. As noted in

section 1, Shen and Wang [15] proposed equation (4), where $\eta_{g0}^{\alpha\beta}$ were arbitrary material parameters not associated with the dislocation type. In APFM [17], which is an 'atomistic' form of PFM, $\eta_{g0}^{\alpha\beta}$ are related to the Shockley partial dislocation core size, among other atomistic-based parameters. This extension was physically motivated because the character angles of the Shockley partials depend on the character angle of the parent full dislocation. For example, an edge and a screw dislocation, respectively, dissociate into two 60° and 30° Shockley partials. In addition, a recent analytical work [34] revealed that the vectorial slip of a partial dislocation may deviate from that of an ideal Shockley partial, $(a_0/6)\langle 112\rangle$. This deviation is more pronounced in a screw dislocation than in an edge dislocation. Since the partial dislocations, to which $\eta_{g0}^{\alpha\beta}$ are related, may have different atomistic structures as the full dislocation character angle changes, it is desirable to extend $\eta_{g0}^{\alpha\beta}$ such that their values depend on the dislocation type. Therefore, for dissociated dislocations in FCC metals in APFM, Mianroodi and Svendsen [17] fit $\eta_{g0}^{\alpha\beta}$ to the MS-based Shockley partial dislocation core structure. Similarly, in one GPN model, $\eta_{g0}^{\alpha\beta}$ were fit to the MS-based disregistry fields [35].

However, in all those works, for the sake of simplicity, a uniform $\eta_{g0}^{\alpha\beta}$ was adopted for all order parameters. In this work, we consider η_{A}^{11} and η_{A}^{22} as independently adjustable parameters. Their characterization will be discussed in section 3.1.

As noted in section 1, all prior PFDD models did not include the gradient energy density in the total energy density. Recently it was shown that introducing atomistically-informed ψ_{gra} into PF-based models, such as APFM, provided descriptions of dislocation cores of pure edge and screw characters closer to those calculated with MS [27, 33]. Therefore, ψ_{gra} is added to the PFDD energy formulation here. As a result, PFDD and APFM, despite employing different slip vectors, are physically equivalent and should yield identical results, as long as all parameters used in the two models are equivalent.

2.2. CAC method

The theoretical foundation of the CAC method is the atomistic field theory (AFT) [36]. In AFT, a crystal is viewed as a continuous collection of lattice points. Embedded within each point is a unit cell containing a group of discrete atoms [37, 38]. In terms of Eulerian coordinates, for monatomic crystals, like Al, in the absence of external force, AFT has the following balance equations [39, 40], i.e.,

$$\frac{\mathrm{d}\rho}{\mathrm{d}t} = -\rho\nabla_{\boldsymbol{x}}\cdot\boldsymbol{v} \tag{9}$$

$$\rho\frac{\mathrm{d}\boldsymbol{v}}{\mathrm{d}t} = \nabla_{\boldsymbol{x}}\cdot\boldsymbol{T} \tag{10}$$

$$\rho\frac{\mathrm{d}e}{\mathrm{d}t} = \nabla_{\boldsymbol{x}}\cdot\boldsymbol{q} + \boldsymbol{T}\cdot\nabla_{\boldsymbol{x}}\boldsymbol{v}, \tag{11}$$

where $\boldsymbol{x}$ is the physical space coordinate of the continuously distributed lattice; ρ, $\boldsymbol{v}$, $\rho\boldsymbol{v}$, and ρe are the density of mass, velocity, linear momentum, and total energy, respectively; $\boldsymbol{T}$ and $\boldsymbol{q}$ are the stress tensor and heat flux vector, respectively.

As a realization of AFT, a CAC model usually consists of two domains: an atomistic domain and a coarse-grained domain, with the interatomic potential being the only constitutive rule [41]. In the atomistic domain, the atoms are updated in the same way as in atomistic simulations; in the coarse-grained domain, finite elements that require neither

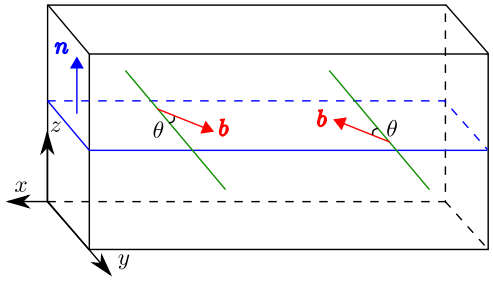

Figure 1. Simulation box set-up for dissociation of a mixed-type dislocation dipole.

displacement continuity nor strain compatibility are employed [42]. Hence, discontinuities such as dislocations and ISFs can be accommodated between two layers of elements [43, 44]. For an FCC lattice, all surfaces of the finite elements lie on {111} planes [45]. The CAC method equipped with these finite elements has been employed to explore problems in which full atomistic resolution is required in some regions (e.g. lattice defects), with coarse-graining employed elsewhere to support representation of dislocation interactions and transport [46, 47]. In this paper, we focus on the modeling of dislocations between finite elements in the coarse-grained domain.

3. Simulation set-up

To maximize comparability, the same embedded-atom method (EAM) potential [48] is used, for the interatomic interactions in MS and CAC simulations, and for material parameters needed in the PF free energy model, including lattice parameter a_0, elastic constants C_{11}, C_{12}, C_{44}, gradient energy coefficients $\eta_{g0}^{\alpha\beta}$, and GSFE per unit area γ_{gsf}.

A dislocation dipole consisting of two dislocations of the same type but with opposite Burgers vector is built into a 3D periodic simulation cell, as illustrated in figure 1. Seven character angles will be considered, including 0° (screw), 15°, 30°, 45°, 60°, 75°, and 90° (edge). Let L_x, L_y, and L_z be the edge length of the cell along the x, y, and z directions, respectively. The two dislocation lines lie on the mid-z plane and are separated by $L_x/2$ along the x direction. In all simulations, the total energy of the dislocated system is minimized, during which each dislocation extends on the mid-z plane by dissociating into two Shockley partials. The center of each partial is determined by projecting the disregistry field onto the partial dislocation direction [33]. The ISF width d is defined as the distance between the centers of two Shockley partial dislocations.

3.1. PFDD and APFM simulations

PF simulations are carried out using a 3D structured grid. In PFDD, 128 grid points are used in each direction; in APFM, the numbers of grid points along the x, y, and z directions are 294, 7, and 180, respectively. Let h_x, h_y, and h_z be the grid spacing along the x, y, and z directions, respectively. Along the same direction, the grid spacing is a constant. Following a prior APFM work [17], $h_z = d_{111}$. Unless stated otherwise, $h_x = h_y = d_{111}$. Note that, since the grid spacing is comparable to the atomic spacing, there is no computational gain with respect to MS. Conceptually, PF-based models have much longer (i.e. diffusive) timescale resolution in comparison to molecular dynamics, but this is not relevant in this work.

Table 1. Lattice parameter a_0 (in Å) and elastic constants C_{11}, C_{12}, C_{44} (in GPa) determined based on the Al EAM potential [48].

a_0	C_{11}	C_{12}	C_{44}
4.05	113.80	61.55	31.60

Table 2. The two gradient energy coefficients in APFM for an extended edge or screw dislocation configuration. The units are μd_{111}^2, where $\mu = (3C_{44} + C_{11} - C_{12})/5$.

	η_A^{11}	η_A^{22}
Screw	0.266 7	0.4
Edge	1.066 7	0.4

Material parameters a_0, C_{11}, C_{12}, and C_{44} enter the free energy model, as summarized in table 1. In prior PFDD modeling, the material was assumed elastic isotropic. Here, to be consistent with APFM, the full anisotropic stiffness tensor $\boldsymbol{C}_E$ is used.

Because the gradient energy density represents the energy of the partial dislocation cores, the gradient energy coefficients, $\eta_{g0}^{\alpha\beta}$, depend on the material and dislocation type, as discussed earlier. Thus, these coefficients need to be characterized for a specific dislocation type in a specific material. In this work, the two independent coefficients in APFM, η_A^{11} and η_A^{22}, are determined by

$$[\eta_A^{11}, \eta_A^{22}] = \text{argmin}\,\{\boldsymbol{\zeta}(\eta_A^{11}, \eta_A^{22}) - \boldsymbol{\zeta}_{MS}\}. \tag{12}$$

Specifically, a series of APFM simulations are performed with a preassigned set of $[\eta_A^{11}, \eta_A^{22}]$. For each simulation, the disregistry field $\boldsymbol{\zeta}(\eta_A^{11}, \eta_A^{22})$ is obtained and compared to that from MS, $\boldsymbol{\zeta}_{MS}$. The values of $[\eta_A^{11}, \eta_A^{22}]$ providing the best agreement for edge and screw dislocations are summarized in table 2. Then, values of the nine coefficients in PFDD are determined following equations (A.20)–(A.22) in the appendix. In this work, we will quantify the effects of ψ_{gra} on mixed-type dislocations by repeating the same PFDD simulations without ψ_{gra}, which will be designated by 'PFDD$_{ng}$'.

In all PF simulations, the elastic energy density ψ_{ela} is calculated by the fast Fourier transform method with the help of Green's functions. Initially, an undissociated perfect dislocation dipole with a given character angle θ is inserted by assigning, $\phi_1^P = 1$ and $\phi_2^P = \phi_3^P = 0$ in PFDD and $\phi_1^A = 1$ and $\phi_2^A = 0$ in APFM, to selected grid points. The dislocation lines remain along the y axis but the slip vectors $\boldsymbol{b}_\alpha$ change directions based on θ. During recursively running the TDGL equation (equation (7)), each dislocation becomes extended. Iterations are terminated when the Euclidean norm of the difference in global vector of each order parameter between successive iterations is smaller than 10^{-4}. The Ginzburg–Landau coefficient m_0 is assumed to be unity and all slips are confined to the pre-defined slip plane [18].

To solve the TDGL equation, the explicit Euler method is used. In this case, we consider the maximum allowable timestep size Δt that stabilizes the iteration [49]. We find that the maximum allowable Δt decreases with (i) a smaller grid spacing, (ii) the inclusion of ψ_{gra}, and (iii) larger gradient energy coefficients $\eta_{g0}^{\alpha\beta}$. Based on a series of parametric studies, we choose $\Delta t = 0.02$ in all PF simulations in this paper.

Table 3. Edge lengths L_x, L_y, and L_z of the MS and CAC simulation cell (in Å) and the corresponding number of atoms N_{atom}, for different dislocation character angle θ.

θ	L_x	L_y	L_z	N_{atom}
0°/60°	515.86	74.46	364.77	843,648
30°/90°	630.03	34.72	420.89	554,400
15°/45°/75°	575.16	143.79	350.74	1,746,600

3.2. MS and CAC simulations

MS and CAC simulations are carried out by LAMMPS [50] and PyCAC [51, 52], respectively. The simulation cell sizes and the corresponding number of atoms are summarized in table 3. In CAC, the coarse-grained domain adopts uniformly sized 3D rhombohedral finite elements. Following PF models, the edge length of a finite element is denoted by h_x, which equals h_y in CAC. In this paper, $h_x = h_y = 4b = 2\sqrt{2}\,a_0$, unless stated otherwise. As a result, each finite element contains 125 atoms and 125 integration points. There is no computational gain with respect to MS.

The interplanar distance between two adjacent finite elements is kept as d_{111} because the finite element boundaries must correspond to actual lattice sites. The Galerkin method is used to convert the balance equations to a set of integration equations, wherein the integration steps are approximated by Gaussian quadrature [53].

In each simulation, an undissociated perfect dislocation dipole is first created by applying the corresponding isotropic elastic displacement field to all atoms/nodes. Then conjugate gradient relaxation is carried out and terminated when one of the following two criteria is satisfied: (i) the change in energy between successive iterations divided by the most recent energy magnitude is less than or equal to 10^{-15} and (ii) the length of the global force vector for all atoms/nodes is less than or equal to 10^{-15} eV Å^{-1}.

4. Results and discussions

Figures 2 and 3 present the calculated disregistry profiles of all seven dislocations based on PFDD_{ng}. As shown, the profiles for the mixed-type dislocations lay between those of the pure-type dislocations. Also, for the same character angle θ, PFDD_{ng} predicts a more compact dislocation core than MS. This discrepancy would imply a need to include the gradient energy density ψ_{gra} in the system free energy. Doing so gives rise to the question: how should the coefficients $\eta_{\text{g0}}^{\alpha\beta}$ be determined for a given θ? On the one hand, table 2 shows that $\eta_{\text{g0}}^{\alpha\beta}$ is different for an edge and a screw dislocation. On the other hand, it is difficult to fit $\eta_{\text{g0}}^{\alpha\beta}$ to all MS-based mixed-type dislocations which can have any θ between 0° and 90°.

Toward a solution, we first note that for a dislocation with a given θ, the associated ISF width d can be approximated to first order by isotropic linear elasticity [1], i.e.,

$$d = \frac{\mu b_{\text{p}}^2}{8\pi(1-\nu)\gamma_{\text{isf}}}[2 - \nu - 2\nu\cos(2\theta)], \tag{13}$$

where γ_{isf} is the ISF energy, and μ and ν are the isotropic shear modulus and Poisson's ratio, respectively. For equation (13), even with Al EAM potential-informed parameters $\gamma_{\text{isf}} = 146\,\text{mJ m}^{-2}$, $\mu = 28$ GPa, and $\nu = 0.3$, we can expect some deviation from the MS results to arise since core field contributions are neglected [54–56]. Further, equation (13)

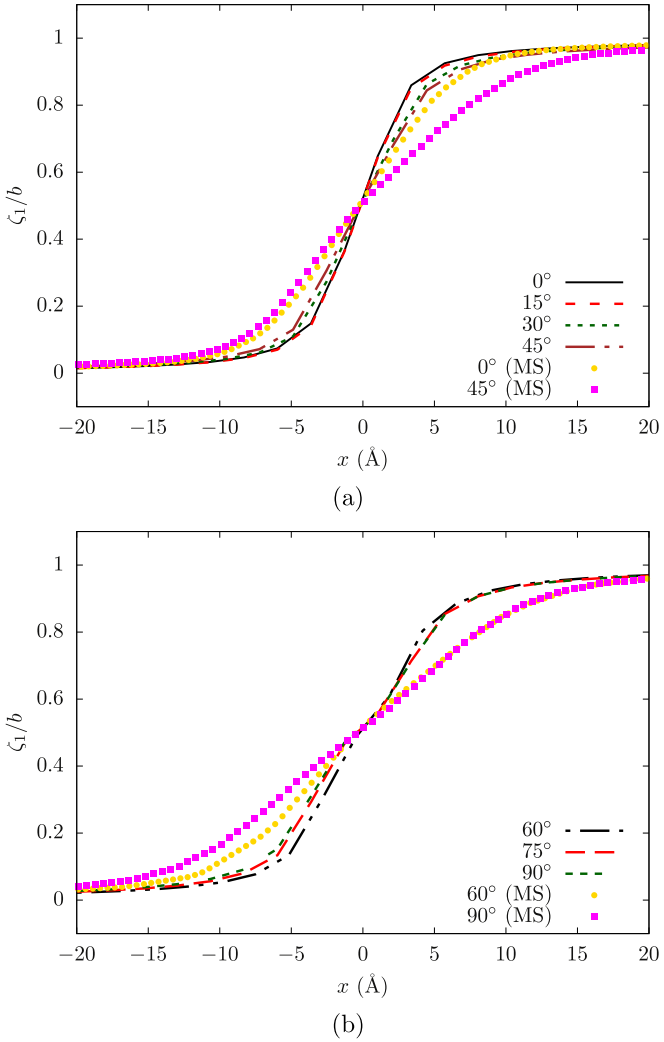

Figure 2. Disregistry fields of pure- and mixed-type dislocations with different character angles along the perfect dislocation Burgers vector direction. Results are based on PFDD_{ng}, where the gradient energy density ψ_{gra} is not included in the system free energy. MS results of some dislocations are also shown for comparison.

suggests that the edge and screw dislocations are two extremes on the spectrum of not only θ but also d. On this basis, we propose that their corresponding gradient energy coefficients $\eta_{\text{g0}}^{\alpha\beta}$ also lie at extreme ends. Accordingly, two interpolation schemes to determine $\eta_{\text{g0}}^{\alpha\beta}$ for mixed-type dislocations are put forth here and compared: a linear interpolation and a trigonometric interpolation, i.e.,

$$\eta_{\text{lin}}^{\alpha\beta}(\theta) = \eta_{\text{S}}^{\alpha\beta} + 2\theta(\eta_{\text{E}}^{\alpha\beta} - \eta_{\text{S}}^{\alpha\beta})/\pi \tag{14}$$

$$\eta_{\text{tri}}^{\alpha\beta}(\theta) = \frac{1}{2}[\eta_{\text{E}}^{\alpha\beta} + \eta_{\text{S}}^{\alpha\beta} - (\eta_{\text{E}}^{\alpha\beta} - \eta_{\text{S}}^{\alpha\beta})\cos(2\theta)], \tag{15}$$

where ‘E’ and ‘S’ denote the edge and screw dislocation, respectively.

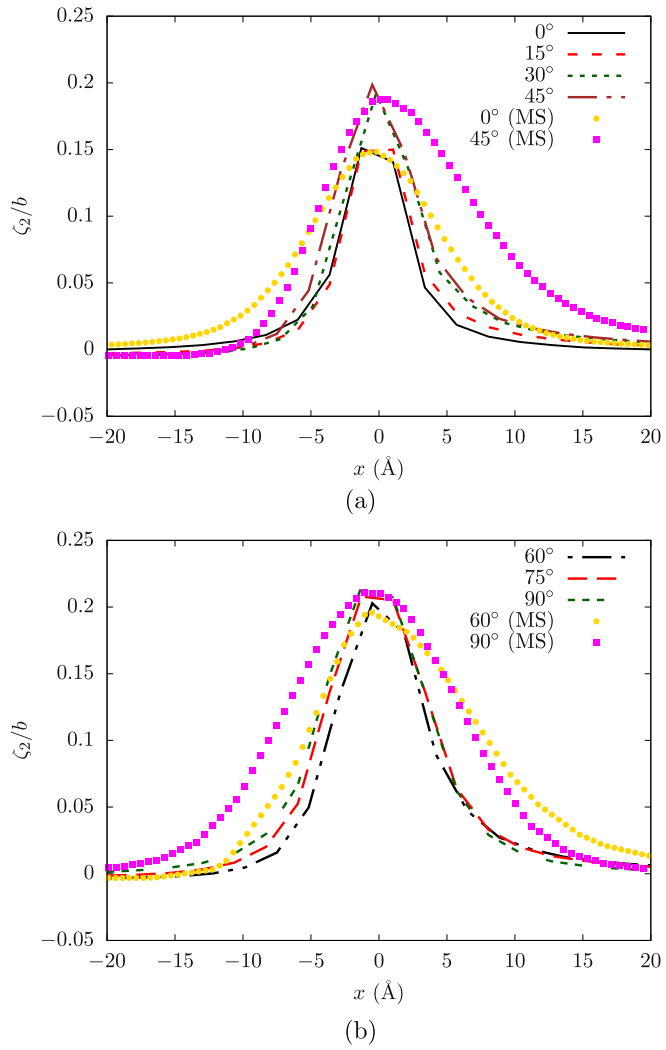

Figure 3. Disregistry fields of pure- and mixed-type dislocations with different character angles normal to the perfect dislocation Burgers vector direction. Results are based on PFDD_{ng}, where the gradient energy density ψ_{gra} is not included in the system free energy. MS results of some dislocations are also shown for comparison.

In our earlier work in Al and Au [33], we found that adding ψ_{gra} to the system free energy causes the dislocations to become more dissociated (i.e. a larger ISF width d) and the disregistry profiles achieve better agreement with the MS results. The present work shows that it is also the case for mixed-type dislocations (figures 4 and 5). This outcome is a result of the fact that it is more energetically favorable for the dislocation to increase d, thereby reducing the interaction energy between the partial dislocations at the expense of increasing the fault area. In addition, results based on the gradient energy-equipped PFDD and APFM are identical, provided that equivalent parameters are used. Moreover, figure 6 shows that, compared with the linear interpolation (equation (14)), results based on the trigonometric interpolation (equation (15)) better agree with MS. This is somewhat expected, because the

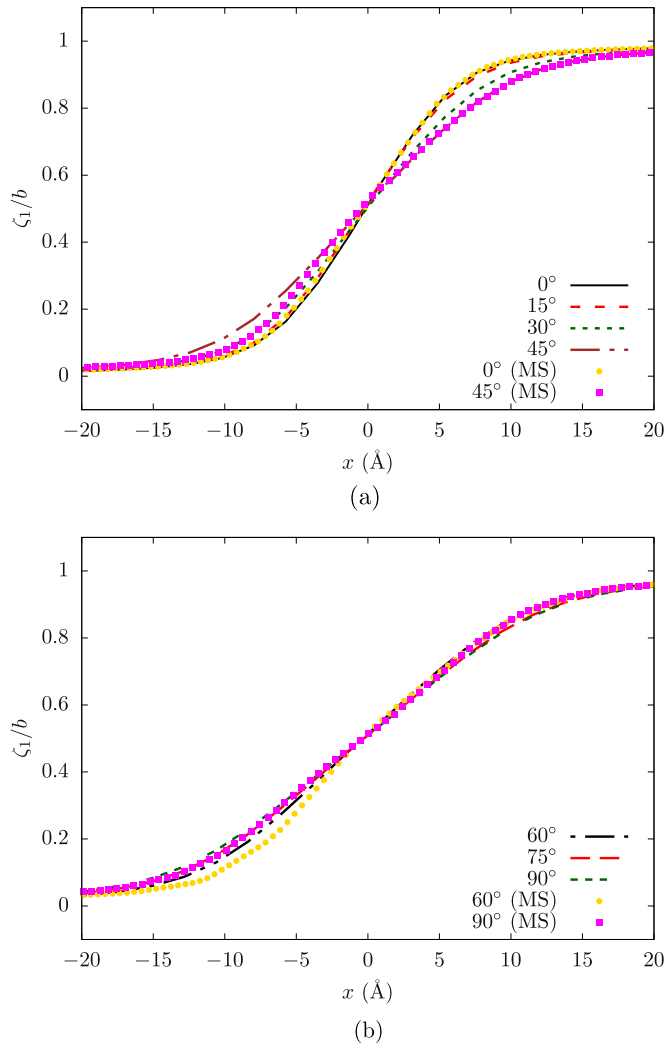

Figure 4. Disregistry fields of pure- and mixed-type dislocations with different character angles along the perfect dislocation Burgers vector direction. Results are based on PFDD, where the gradient energy density ψ_{gra} is included in the system free energy and the coefficients $\eta_{\text{g0}}^{\alpha\beta}$ for mixed-type dislocations are interpolated from those of edge and screw ones by equation (15). MS results of some dislocations are also shown for comparison.

character angle of a Shockley partial dislocation changes trigonometrically as the character angle of the full dislocation varies. Thus, only PFDD results are discussed further in what follows and the trigonometric interpolation scheme is used in the remainder of this paper.

In addition to the disregistry fields, we also compare the stress fields predicted by different models. Consider the 30° and 45° mixed-type dislocations as an example. Figure 7 shows that, introducing gradient energy to total energy in PFDD improves the agreement in the stress fields with those of MS. Note that, however, the virial stresses obtained in CAC and MS may have different physical meaning than those in continuum-based (e.g. PF) models [57, 58]. Work is

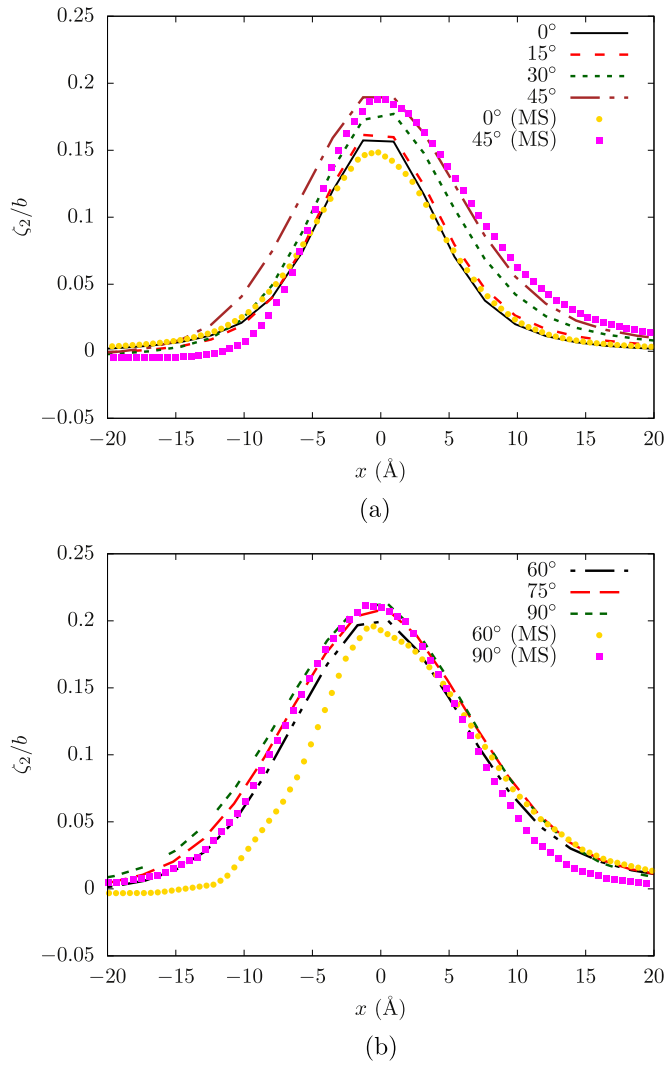

Figure 5. Disregistry fields of pure- and mixed-type dislocations with different character angles normal to the perfect dislocation Burgers vector direction. Results are based on PFDD, where the gradient energy density ψ_{gra} is included in the system free energy and the coefficients $\eta_{\text{g0}}^{\alpha\beta}$ for mixed-type dislocations are interpolated from those of edge and screw ones by equation (15). MS results of some dislocations are also shown for comparison.

underway to develop an atomic stress formulation that is directly comparable to the continuum stress.

In foregoing PFDD simulations, the number of grid points along each direction, $N_{\text{gp}} = 128$. To show that the cell size is sufficiently large, we vary N_{gp} from 80 to 160, and calculated the ISF widths for all seven dislocations. Figure 8 presents the difference in the ISF width between the smaller N_{gp} with $N_{\text{gp}} = 160$. It is found that, for the same dislocation, the difference reduces to less than $0.01b$ when $N_{\text{gp}} = 128$, suggesting that the maximum relative error is about 1%.

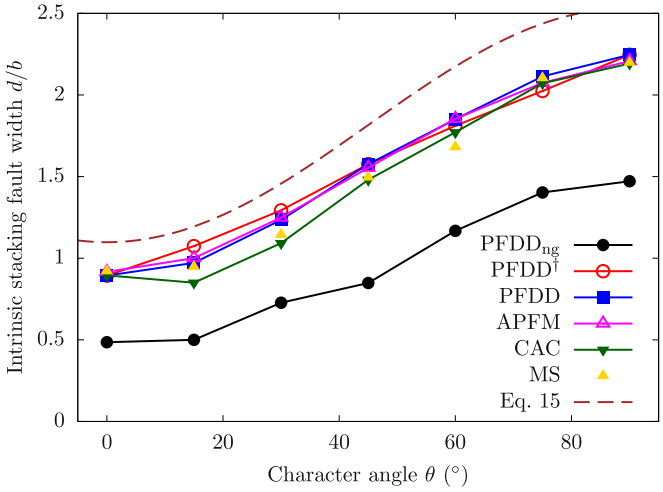

Figure 6. ISF widths, d, predicted by PFDD, APFM, CAC, and MS simulations, for seven dislocations with different character angle θ. Isotropic linear elasticity prediction in equation (13) is also shown. PFDD$_{ng}$ refers to the PFDD variant without the gradient energy in the system free energy; PFDD† and PFDD, respectively, refer to the gradient energy-equipped PFDD variants with the linear (equation (14)) and trigonometric (equation (15)) interpolation schemes for the coefficients $\eta_{g0}^{\alpha\beta}$ for mixed-type dislocations. Results based on APFM are identical to those of PFDD.

In the foregoing simulations, $h_x = h_y = h_z = d_{111}$ in PFDD, and $h_x = h_y = 4b$ and $h_z = d_{111}$ in CAC. From a numerical perspective, it is important to understand the effects of space resolution on simulation results. Here, we examine the influences of the in-plane grid spacing. First, we find that in PFDD, varying the grid spacing along the dislocation line direction, h_y, results in unchanged disregistry fields, suggesting that the effects of the in-slip-plane grid spacing are dominated by h_x. It follows that, we keep $h_z = d_{111}$ and vary h_x and h_y simultaneously in both PFDD and CAC. Figure 9 shows that, larger h_x and h_y result in a larger d in CAC but a smaller d in PFDD. In PFDD, the dependence of h_x axis stronger for screw-like dislocations than edge-like dislocations. When $h_x > 4b$, PFDD-predicted values for d are nearly zero. As h_x in the simulation decreases to the MS-based ISF width, d_{MS}, approximately between b and $2b$, the PFDD-predicted d quickly approaches d_{MS}. This is expected because (i) the dislocation core can be resolved only when $h_x \leqslant d_{MS}$ and (ii) the gradient energy coefficients calibrated against MS are suitable only for simulations at atomic or subatomic resolution. As h_x decreases further yields, the results slowly converge.

5. Conclusions

In this paper, three continuum dislocation models—PFDD, APFM, and CAC—are employed to simulate static pure- and mixed-type dislocation core structures in FCC Al. Seven dislocations, with the character angle ranging from 0°, 15°, 30°, 45°, 60°, 75°, to 90°, are considered. In PFDD, the gradient energy density is added to the system free energy for the first time. In both PFDD and APFM, the gradient energy coefficients are extended, from a uniform parameter to independently adjustable ones, to achieve a better description of the dislocation core structure. A trigonometric interpolation scheme is proposed to obtain the

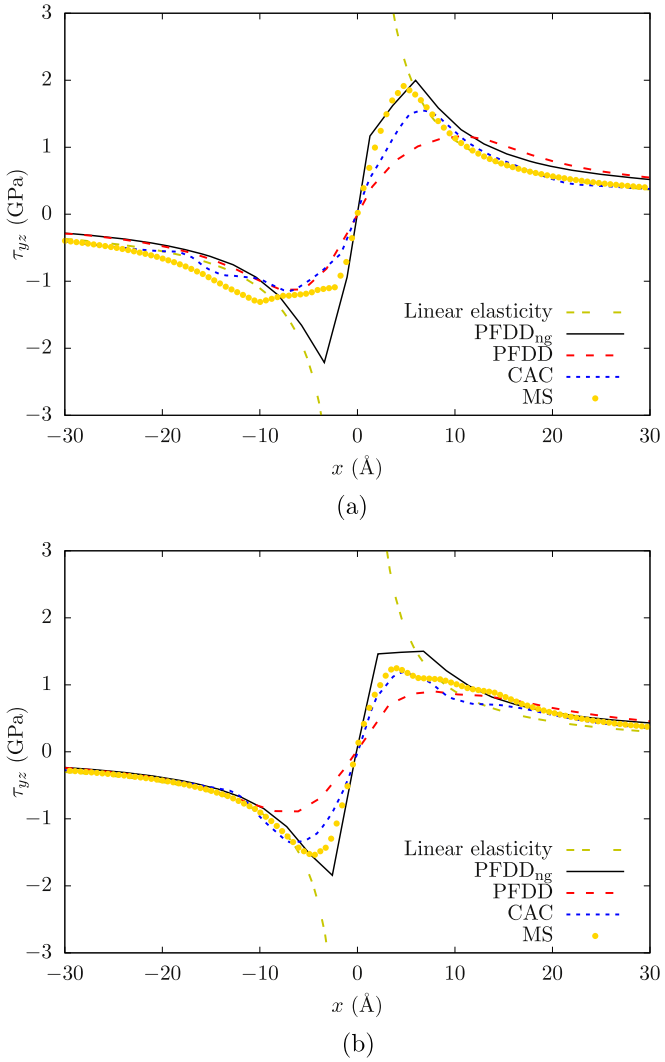

Figure 7. The yz component of the stress tensor of the (a) 30° and (b) 45° mixed-type dislocations. PFDD$_{ng}$ refers to the PFDD variant without the gradient energy in the system free energy. PFDD and PFDD$_{ng}$ results are based on the trigonometric interpolation scheme (equation (15)) for the gradient energy coefficients $\eta_{g0}^{\alpha\beta}$ for mixed-type dislocations.

gradient energy coefficients for mixed-type dislocations from those for pure-type ones. The effects of the in-slip-plane space numerical resolution on predicted disregistry profiles are analyzed. Our results suggest that, in the case of a straight dislocation, for PFDD and APFM results to be comparable with MS, subatomic or atomic resolution should be applied within the plane that is normal to the dislocation line. The general agreement between MS and PFDD/APFM/CAC simulations for straight dislocations lays a solid foundation for applying the latter set of methods to more complex and practical problems, such as curved dislocations

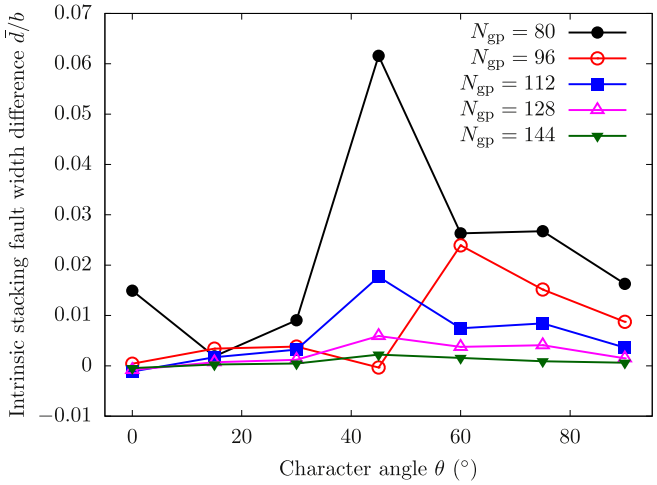

Figure 8. N_{gp} is the number of grid points along each direction in PFDD simulation cells. $\bar{d}$ is the difference in the ISF width predicted in cells with different N_{gp} with respect to that in with $N_{gp} = 160$, for seven dislocations with different character angle θ. Results are based on the trigonometric interpolation scheme (equation (15)) for the coefficients $\eta_{g0}^{\alpha\beta}$ for mixed-type dislocations.

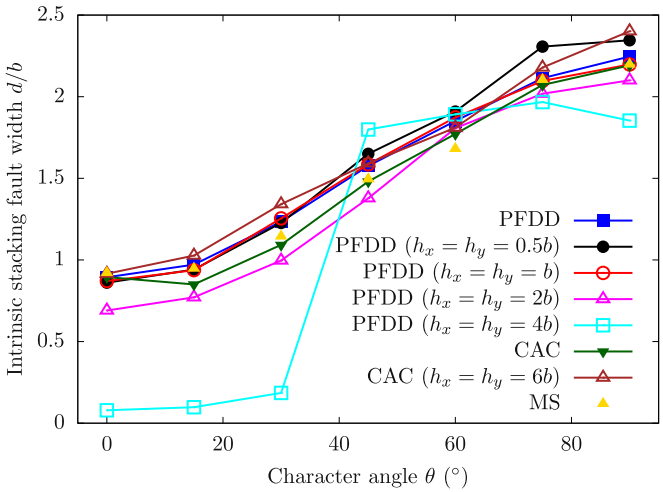

Figure 9. ISF widths, d, predicted by PFDD and CAC simulations with different in-plane grid spacings or finite element sizes, for seven dislocations with different character angle θ. Unless stated otherwise, $h_x = h_y = h_z = d_{111}$ in PFDD and $h_x = h_y = 4b$ in CAC. MS results are also shown for comparison. PFDD results are based on the trigonometric interpolation scheme (equation (15)) for the gradient energy coefficients $\eta_{g0}^{\alpha\beta}$ for mixed-type dislocations.

and dislocation loops. Future work also includes extending PFDD to body-centered cubic (BCC) lattice. With this in mind, further comparison between PFDD and a recent extension of CAC to dislocation modeling in a BCC lattice [59] is expected.

Acknowledgments

We thank Dr Yang Xiang and Dr Jaehyun Cho for helpful discussions. The work of SX was supported in part by the Elings Prize Fellowship in Science offered by the California NanoSystems Institute on the UC Santa Barbara campus. SX, LS, and IJB gratefully acknowledge support from the Office of Naval Research under contract ONR BRC Grant N00014-18-1-2392. JRM and BS gratefully acknowledge partial support from the Deutsche Forschungsgemeinschaft (DFG) through Subproject M5 (M8) in the Priority Programme 1713. AH gratefully acknowledges support from the Materials project within the Physics and Engineering Models (PEM) Subprogram element of the Advanced Simulation and Computing (ASC) Program at Los Alamos National Laboratory (LANL). Use was made of computational facilities purchased with funds from the National Science Foundation (CNS-1725797) and administered by the Center for Scientific Computing (CSC). The CSC is supported by the California NanoSystems Institute and the Materials Research Science and Engineering Center (MRSEC; NSF DMR 1720256) at UC Santa Barbara. This work used the Extreme Science and Engineering Discovery Environment (XSEDE), which is supported by National Science Foundation grant number ACI-1053575.

Appendix

In the current work of a single slip plane, $d_\alpha = d_\beta = d_0$, substituting equation (6) into equation (4) yields

$$\psi_{\text{gra}}(\nabla\boldsymbol{\phi}) = \frac{1}{d_0^2}\sum_{\alpha,\beta=1}^{n}\eta_{\text{g0}}^{\alpha\beta}\boldsymbol{b}_\alpha\cdot\boldsymbol{b}_\beta\nabla\phi_\alpha\cdot\boldsymbol{N}_0\nabla\phi_\beta, \tag{A.1}$$

where $\boldsymbol{N}_0 = [(\boldsymbol{n}_\alpha\cdot\boldsymbol{n}_\beta)\boldsymbol{I} - \boldsymbol{n}_\beta\otimes\boldsymbol{n}_\alpha]$ is the same for all sets of $\alpha\beta$ because $\boldsymbol{n}_\alpha = \boldsymbol{n}_\beta$. Below, subscripts or superscripts A and P denote quantities in APFM and PFDD, respectively. Our earlier work [33] showed that

$$\boldsymbol{b}_1^{\text{A}} = \boldsymbol{b}_1^{\text{P}} \tag{A.2}$$

$$\boldsymbol{b}_2^{\text{A}} = \boldsymbol{b}_2^{\text{P}} - \boldsymbol{b}_3^{\text{P}} \tag{A.3}$$

$$\phi_1^{\text{A}} = \phi_1^{\text{P}} - \frac{1}{2}(\phi_2^{\text{P}} + \phi_3^{\text{P}}) \tag{A.4}$$

$$\phi_2^{\text{A}} = \frac{1}{2}(\phi_2^{\text{P}} - \phi_3^{\text{P}}). \tag{A.5}$$

It follows that

$$\nabla\phi_1^{\text{A}} = \nabla\phi_1^{\text{P}} - \frac{1}{2}(\nabla\phi_2^{\text{P}} + \nabla\phi_3^{\text{P}}) \tag{A.6}$$

$$\nabla\phi_2^{\text{A}} = \frac{1}{2}(\nabla\phi_2^{\text{P}} - \nabla\phi_3^{\text{P}}). \tag{A.7}$$

In APFM, $\boldsymbol{b}_a^{\text{A}}\cdot\boldsymbol{b}_b^{\text{A}} = 0$ when $a \neq b$, hence there are two independent coefficients η_{A}^{11} and η_{A}^{22}, and equation (A.1) becomes

$$\psi_{\text{gra}}(\nabla\boldsymbol{\phi}) = \frac{1}{d_0^2}(\eta_{\text{A}}^{11}\boldsymbol{b}_1^{\text{A}}\cdot\boldsymbol{b}_1^{\text{A}}\nabla\phi_1^{\text{A}}\cdot\boldsymbol{N}_0\nabla\phi_1^{\text{A}} + \eta_{\text{A}}^{22}\boldsymbol{b}_2^{\text{A}}\cdot\boldsymbol{b}_2^{\text{A}}\nabla\phi_2^{\text{A}}\cdot\boldsymbol{N}_0\nabla\phi_2^{\text{A}}). \tag{A.8}$$

Substituting equations (A.2), (A.3), (A.6), and (A.7) into equation (A.8) yields

$$\psi_{\mathrm{gra}}(\nabla\boldsymbol{\phi}) = \frac{1}{d_0^2}(\eta_{\mathrm{A}}^{11}\boldsymbol{b}_1^{\mathrm{P}}\cdot\boldsymbol{b}_1^{\mathrm{P}}\left[\nabla\phi_1^{\mathrm{P}} - \frac{1}{2}(\nabla\phi_2^{\mathrm{P}} + \nabla\phi_3^{\mathrm{P}})\right]\cdot\boldsymbol{N}_0\left[\nabla\phi_1^{\mathrm{P}} - \frac{1}{2}(\nabla\phi_2^{\mathrm{P}} + \nabla\phi_3^{\mathrm{P}})\right] + \eta_{\mathrm{A}}^{22}(\boldsymbol{b}_2^{\mathrm{P}} - \boldsymbol{b}_3^{\mathrm{P}})\cdot(\boldsymbol{b}_2^{\mathrm{P}} - \boldsymbol{b}_3^{\mathrm{P}})\left[\frac{1}{2}(\nabla\phi_2^{\mathrm{P}} - \nabla\phi_3^{\mathrm{P}})\right]\cdot\boldsymbol{N}_0\left[\frac{1}{2}(\nabla\phi_2^{\mathrm{P}} - \nabla\phi_3^{\mathrm{P}})\right]. \tag{A.9}$$

On the other hand, equation (A.8) equals its equivalent in PFDD, i.e.,

$$\psi_{\mathrm{gra}}(\nabla\boldsymbol{\phi}) = \frac{1}{d_0^2}\sum_{\alpha,\beta=1}^{3}\eta_{\mathrm{P}}^{\alpha\beta}\boldsymbol{b}_\alpha^{\mathrm{P}}\cdot\boldsymbol{b}_\beta^{\mathrm{P}}\nabla\phi_\alpha^{\mathrm{P}}\cdot\boldsymbol{N}_0\nabla\phi_\beta^{\mathrm{P}}. \tag{A.10}$$

In other words, each of the nine terms in equation (A.9) that contains $(\nabla\phi_\alpha^{\mathrm{P}}\cdot\boldsymbol{N}_0\nabla\phi_\beta^{\mathrm{P}})$ should equal its counterpart in equation (A.10). In specific, in equation (A.9),

- when $\alpha = 1$, $\beta = 1$, the relevant term is
$$\eta_{\mathrm{A}}^{11}\boldsymbol{b}_1^{\mathrm{P}}\cdot\boldsymbol{b}_1^{\mathrm{P}}\nabla\phi_1^{\mathrm{P}}\cdot\boldsymbol{N}_0\nabla\phi_1^{\mathrm{P}}, \tag{A.11}$$
so $\eta_{\mathrm{P}}^{11} = \eta_{\mathrm{A}}^{11}$;
- when $\alpha = 1$, $\beta = 2$, the relevant term is
$$\eta_{\mathrm{A}}^{11}\boldsymbol{b}_1^{\mathrm{P}}\cdot\boldsymbol{b}_1^{\mathrm{P}}\nabla\phi_1^{\mathrm{P}}\cdot\boldsymbol{N}_0\left(-\frac{1}{2}\right)\nabla\phi_2^{\mathrm{P}}, \tag{A.12}$$
which, along with $\boldsymbol{b}_1^{\mathrm{P}}\cdot\boldsymbol{b}_1^{\mathrm{P}} = -2\boldsymbol{b}_1^{\mathrm{P}}\cdot\boldsymbol{b}_2^{\mathrm{P}}$, leads to $\eta_{\mathrm{P}}^{12} = \eta_{\mathrm{A}}^{11}$;
- when $\alpha = 1$, $\beta = 3$, the relevant term is
$$\eta_{\mathrm{A}}^{11}\boldsymbol{b}_1^{\mathrm{P}}\cdot\boldsymbol{b}_1^{\mathrm{P}}\nabla\phi_1^{\mathrm{P}}\cdot\boldsymbol{N}_0\left(-\frac{1}{2}\right)\nabla\phi_3^{\mathrm{P}}, \tag{A.13}$$
which, along with $\boldsymbol{b}_1^{\mathrm{P}}\cdot\boldsymbol{b}_1^{\mathrm{P}} = -2\boldsymbol{b}_1^{\mathrm{P}}\cdot\boldsymbol{b}_3^{\mathrm{P}}$, leads to $\eta_{\mathrm{P}}^{13} = \eta_{\mathrm{A}}^{11}$;
- when $\alpha = 2$, $\beta = 1$, the relevant term is
$$\eta_{\mathrm{A}}^{11}\boldsymbol{b}_1^{\mathrm{P}}\cdot\boldsymbol{b}_1^{\mathrm{P}}\left(-\frac{1}{2}\right)\nabla\phi_2^{\mathrm{P}}\cdot\boldsymbol{N}_0\nabla\phi_1^{\mathrm{P}}, \tag{A.14}$$
which, along with $\boldsymbol{b}_1^{\mathrm{P}}\cdot\boldsymbol{b}_1^{\mathrm{P}} = -2\boldsymbol{b}_2^{\mathrm{P}}\cdot\boldsymbol{b}_1^{\mathrm{P}}$, leads to $\eta_{\mathrm{P}}^{21} = \eta_{\mathrm{A}}^{11}$;
- when $\alpha = 2$, $\beta = 2$, the relevant terms are
$$\eta_{\mathrm{A}}^{11}\boldsymbol{b}_1^{\mathrm{P}}\cdot\boldsymbol{b}_1^{\mathrm{P}}\left(-\frac{1}{2}\right)\nabla\phi_2^{\mathrm{P}}\cdot\boldsymbol{N}_0\left(-\frac{1}{2}\right)\nabla\phi_2^{\mathrm{P}} + \eta_{\mathrm{A}}^{22}(\boldsymbol{b}_2^{\mathrm{P}} - \boldsymbol{b}_3^{\mathrm{P}})\cdot(\boldsymbol{b}_2^{\mathrm{P}} - \boldsymbol{b}_3^{\mathrm{P}})\frac{1}{2}\nabla\phi_2^{\mathrm{P}}\cdot\boldsymbol{N}_0\frac{1}{2}\nabla\phi_2^{\mathrm{P}}, \tag{A.15}$$
which, along with $\boldsymbol{b}_1^{\mathrm{P}}\cdot\boldsymbol{b}_1^{\mathrm{P}} = (\boldsymbol{b}_2^{\mathrm{P}} - \boldsymbol{b}_3^{\mathrm{P}})\cdot(\boldsymbol{b}_2^{\mathrm{P}} - \boldsymbol{b}_3^{\mathrm{P}})/3 = \boldsymbol{b}_2^{\mathrm{P}}\cdot\boldsymbol{b}_2^{\mathrm{P}}$, leads to $\eta_{\mathrm{P}}^{22} = \eta_{\mathrm{A}}^{11}/4 + 3\eta_{\mathrm{A}}^{22}/4$;
- when $\alpha = 2$, $\beta = 3$, the relevant terms are
$$\eta_{\mathrm{A}}^{11}\boldsymbol{b}_1^{\mathrm{P}}\cdot\boldsymbol{b}_1^{\mathrm{P}}\left(-\frac{1}{2}\right)\nabla\phi_2^{\mathrm{P}}\cdot\boldsymbol{N}_0\left(-\frac{1}{2}\right)\nabla\phi_3^{\mathrm{P}} + \eta_{\mathrm{A}}^{22}(\boldsymbol{b}_2^{\mathrm{P}} - \boldsymbol{b}_3^{\mathrm{P}})\cdot(\boldsymbol{b}_2^{\mathrm{P}} - \boldsymbol{b}_3^{\mathrm{P}})\frac{1}{2}\nabla\phi_2^{\mathrm{P}}\cdot\boldsymbol{N}_0\left(-\frac{1}{2}\right)\nabla\phi_3^{\mathrm{P}}, \tag{A.16}$$
which, along with $\boldsymbol{b}_1^{\mathrm{P}}\cdot\boldsymbol{b}_1^{\mathrm{P}} = (\boldsymbol{b}_2^{\mathrm{P}} - \boldsymbol{b}_3^{\mathrm{P}})\cdot(\boldsymbol{b}_2^{\mathrm{P}} - \boldsymbol{b}_3^{\mathrm{P}})/3 = -2\boldsymbol{b}_2^{\mathrm{P}}\cdot\boldsymbol{b}_3^{\mathrm{P}}$, leads to $\eta_{\mathrm{P}}^{23} = -\eta_{\mathrm{A}}^{11}/2 + 3\eta_{\mathrm{A}}^{22}/2$;

- when $\alpha = 3$, $\beta = 1$, the relevant term is

$$\eta_{\mathrm{A}}^{11}\boldsymbol{b}_1^{\mathrm{P}} \cdot \boldsymbol{b}_1^{\mathrm{P}}\left(-\frac{1}{2}\right)\nabla\phi_3^{\mathrm{P}} \cdot \boldsymbol{N}_0\nabla\phi_1^{\mathrm{P}}, \tag{A.17}$$

  which, along with $\boldsymbol{b}_1^{\mathrm{P}} \cdot \boldsymbol{b}_1^{\mathrm{P}} = -2\boldsymbol{b}_3^{\mathrm{P}} \cdot \boldsymbol{b}_1^{\mathrm{P}}$, leads to $\eta_{\mathrm{P}}^{31} = \eta_{\mathrm{A}}^{11}$;
- when $\alpha = 3$, $\beta = 2$, the relevant terms are

$$\eta_{\mathrm{A}}^{11}\boldsymbol{b}_1^{\mathrm{P}} \cdot \boldsymbol{b}_1^{\mathrm{P}}\left(-\frac{1}{2}\right)\nabla\phi_3^{\mathrm{P}} \cdot \boldsymbol{N}_0\left(-\frac{1}{2}\right)\nabla\phi_2^{\mathrm{P}} + \eta_{\mathrm{A}}^{22}(\boldsymbol{b}_2^{\mathrm{P}} - \boldsymbol{b}_3^{\mathrm{P}}) \cdot (\boldsymbol{b}_2^{\mathrm{P}} - \boldsymbol{b}_3^{\mathrm{P}})\left(-\frac{1}{2}\right)\nabla\phi_3^{\mathrm{P}} \cdot \boldsymbol{N}_0\frac{1}{2}\nabla\phi_2^{\mathrm{P}}, \tag{A.18}$$

  which, along with $\boldsymbol{b}_1^{\mathrm{P}} \cdot \boldsymbol{b}_1^{\mathrm{P}} = (\boldsymbol{b}_2^{\mathrm{P}} - \boldsymbol{b}_3^{\mathrm{P}}) \cdot (\boldsymbol{b}_2^{\mathrm{P}} - \boldsymbol{b}_3^{\mathrm{P}})/3 = -2\boldsymbol{b}_3^{\mathrm{P}} \cdot \boldsymbol{b}_2^{\mathrm{P}}$, leads to $\eta_{\mathrm{P}}^{32} = -\eta_{\mathrm{A}}^{11}/2 + 3\eta_{\mathrm{A}}^{22}/2$;
- when $\alpha = 3$, $\beta = 3$, the relevant terms are

$$\eta_{\mathrm{A}}^{11}\boldsymbol{b}_1^{\mathrm{P}} \cdot \boldsymbol{b}_1^{\mathrm{P}}\left(-\frac{1}{2}\right)\nabla\phi_3^{\mathrm{P}} \cdot \boldsymbol{N}_0\left(-\frac{1}{2}\right)\nabla\phi_3^{\mathrm{P}} + \eta_{\mathrm{A}}^{22}(\boldsymbol{b}_2^{\mathrm{P}} - \boldsymbol{b}_3^{\mathrm{P}}) \cdot (\boldsymbol{b}_2^{\mathrm{P}} - \boldsymbol{b}_3^{\mathrm{P}})\left(-\frac{1}{2}\right)\nabla\phi_2^{\mathrm{P}} \cdot \boldsymbol{N}_0\left(-\frac{1}{2}\right)\nabla\phi_2^{\mathrm{P}}, \tag{A.19}$$

  which, along with $\boldsymbol{b}_1^{\mathrm{P}} \cdot \boldsymbol{b}_1^{\mathrm{P}} = (\boldsymbol{b}_2^{\mathrm{P}} - \boldsymbol{b}_3^{\mathrm{P}}) \cdot (\boldsymbol{b}_2^{\mathrm{P}} - \boldsymbol{b}_3^{\mathrm{P}})/3 = \boldsymbol{b}_3^{\mathrm{P}} \cdot \boldsymbol{b}_3^{\mathrm{P}}$, leads to $\eta_{\mathrm{P}}^{33} = \eta_{\mathrm{A}}^{11}/4 + 3\eta_{\mathrm{A}}^{22}/4$.

In summary,

$$\eta_{\mathrm{P}}^{11} = \eta_{\mathrm{P}}^{12} = \eta_{\mathrm{P}}^{13} = \eta_{\mathrm{P}}^{21} = \eta_{\mathrm{P}}^{31} = \eta_{\mathrm{A}}^{11} \tag{A.20}$$

$$\eta_{\mathrm{P}}^{22} = \eta_{\mathrm{P}}^{33} = \eta_{\mathrm{A}}^{11}/4 + 3\eta_{\mathrm{A}}^{22}/4 \tag{A.21}$$

$$\eta_{\mathrm{P}}^{23} = \eta_{\mathrm{P}}^{32} = -\eta_{\mathrm{A}}^{11}/2 + 3\eta_{\mathrm{A}}^{22}/2. \tag{A.22}$$

Note that the current gradient energy model does not take into account the material symmetry, and so η_{P}^{11}, η_{P}^{22}, and η_{P}^{33} may differ.

ORCID iDs

Shuozhi Xu https://orcid.org/0000-0003-0121-9445
Jaber R Mianroodi https://orcid.org/0000-0003-4778-3260
Abigail Hunter https://orcid.org/0000-0002-0443-4020

References

[1] Hull D and Bacon D J 2011 *Introduction to Dislocations* 5th edn (Butterworth-Heinemann)
[2] Xu S, Rigelesaiyin J, Xiong L, Chen Y and McDowell D L 2018 Generalized continua concepts in coarse-graining atomistic simulations *Generalized Models and Non-classical Approaches in Complex Materials 2, Advanced Structured Materials* (Cham: Springer) pp 237–60
[3] Olmsted D L, Hector L G Jr, Curtin W A and Clifton R J 2005 Atomistic simulations of dislocation mobility in Al, Ni and Al/Mg alloys *Modelling Simul. Mater. Sci. Eng.* **13** 371
[4] Cho J, Junge T, Molinari J-F and Anciaux G 2015 Toward a 3d coupled atomistic and discrete dislocation dynamics simulation: dislocation core structures and Peierls stresses with several character angles in FCC aluminum *Adv. Model. Simul. Eng. Sci.* **2** 12

[5] Cho J, Molinari J-F and Anciaux G 2017 Mobility law of dislocations with several character angles and temperatures in FCC aluminum *Int. J. Plast.* **90** 66–75
[6] Zhou X W, Sills R B, Ward D K and Karnesky R A 2017 Atomistic calculations of dislocation core energy in aluminium *Phys. Rev.* B **95** 054112
[7] Burbery N, Das R and Ferguson W G 2017 Dynamic behaviour of mixed dislocations in FCC metals under multi-oriented loading with molecular dynamics simulations *Comput. Mater. Sci.* **137** 39–54
[8] Dang K and Spearot D 2018 Pressure dependence of the Peierls stress in aluminum *JOM* **70** 1094–9
[9] Dang K, Bamney D, Bootsita K, Capolungo L and Spearot D E 2019 Mobility of dislocations in aluminum: faceting and asymmetry during nanoscale dislocation shear loop expansion *Acta Mater.* **168** 426–35
[10] Xu S and Chen X 2019 Modeling dislocations and heat conduction in crystalline materials: atomistic/continuum coupling approaches *Int. Mater. Rev.* 407–38
[11] Chavoshi S Z and Xu S 2019 Nanoindentation/scratching at finite temperatures: insights from atomistic-based modeling *Prog. Mater. Sci.* **100** 1–20
[12] Wang Y and Li J 2010 Phase field modeling of defects and deformation *Acta Mater.* **58** 1212–35
[13] Khachaturyan A G 2000 Prospects of 3-dimensional nanoscale modeling of engineering materials *Science of Alloys for the XXI Century, TMS Proc. Hume-Rothery Symp.* ed E A Turchi pp 293–308
[14] Wang Y U, Jin Y M, Cuitiño A M and Khachaturyan A G 2001 Nanoscale phase field microelasticity theory of dislocations: model and 3d simulations *Acta Mater.* **49** 1847–57
[15] Shen C and Wang Y 2003 Phase field model of dislocation networks *Acta Mater.* **51** 2595–610
[16] Shen C and Wang Y 2004 Incorporation of γ-surface to phase field model of dislocations: simulating dislocation dissociation in fcc crystals *Acta Mater.* **52** 683–91
[17] Mianroodi J R and Svendsen B 2015 Atomistically determined phase field modeling of dislocation dissociation, stacking fault formation, dislocation slip, and reactions in fcc systems *J. Mech. Phys. Solids* **77** 109–22
[18] Shen C, Li J and Wang Y 2014 Predicting structure and energy of dislocations and grain boundaries *Acta Mater.* **74** 125–31
[19] Zheng S, Zheng D, Ni Y and He L 2018 Improved phase field model of dislocation intersections *npj Comput. Mater.* **4** 20
[20] Koslowski M, Cuitiño A M and Ortiz M 2002 A phase-field theory of dislocation dynamics, strain hardening and hysteresis in ductile single crystals *J. Mech. Phys. Solids* **50** 2597–635
[21] Koslowski M and Ortiz M 2004 A multi-phase field model of planar dislocation networks *Modelling Simul. Mater. Sci. Eng.* **12** 1087–97
[22] Lei L and Koslowski M 2011 Mesoscale modeling of dislocations in molecular crystals *Phil. Mag.* **91** 865–78
[23] Lee D W, Kim H, Strachan A and Koslowski M 2011 Effect of core energy on mobility in a continuum dislocation model *Phys. Rev.* B **83** 104101
[24] Hunter A, Saied F, Le C and Koslowski M 2011 Large-scale 3d phase field dislocation dynamics simulations on high-performance architectures *Int. J. High Perform. Comput. Appl.* **25** 223–35
[25] Hunter A, Beyerlein I J, Germann T C and Koslowski M 2011 Influence of the stacking fault energy surface on partial dislocations in fcc metals with a three dimensional phase field dynamics model *Phys. Rev.* B **84** 144108
[26] Beyerlein I J and Hunter A 2016 Understanding dislocation mechanics at the mesoscale using phase field dislocation dynamics *Phil. Trans. R. Soc.* A **374** 20150166
[27] Mianroodi J R, Hunter A, Beyerlein I and Svendsen B 2016 Theoretical and computational comparison of models for dislocation dissociation and stacking fault/core formation in fcc crystals *J. Mech. Phys. Solids* **95** 719–41
[28] Xiang Y, Wei H, Ming P and E W 2008 A generalized Peirls-Nabarro model for curved dislocations and core structures of dislocation loops in Al and Cu *Acta Mater.* **56** 1447–60
[29] Xiong L, Tucker G, McDowell D L and Chen Y 2011 Coarse-grained atomistic simulation of dislocations *J. Mech. Phys. Solids* **59** 160–77
[30] Xu S, Che R, Xiong L, Chen Y and McDowell D L 2015 A quasistatic implementation of the concurrent atomistic-continuum method for FCC crystals *Int. J. Plast.* **72** 91–126
[31] Hunter A and Beyerlein I J 2013 Unprecedented grain size effect on stacking fault width *APL Mater.* **1** 032109

[32] Hunter A and Beyerlein I J 2014 Stacking fault emission from grain boundaries: material dependencies and grain size effects *Mater. Sci. Eng.* A **600** 200–10
[33] Xu S, Mianroodi J R, Hunter A, Beyerlein I J and Svendsen B 2019 Phase-field-based calculations of the disregistry fields of static extended dislocations in FCC metals *Phil. Mag.* **99** 1400–28
[34] Szajewski B A, Hunter A and Luscher D J 2018 Analytic model of the γ-surface deviation and influence on the stacking fault width between partial dislocations *Comput. Mater. Sci.* **147** 243–50
[35] Liu G, Cheng X, Wang J, Chen K and Shen Y 2016 Peierls stress in face-centered-cubic metals predicted from an improved semi-discrete variation Peierls-Nabarro model *Scr. Mater.* **120** 94–7
[36] Chen Y 2009 Reformulation of microscopic balance equations for multiscale materials modeling *J. Chem. Phys.* **130** 134706
[37] Xu S, Xiong L, Chen Y and McDowell D L 2016 Sequential slip transfer of mixed-character dislocations across $\Sigma 3$ coherent twin boundary in FCC metals: a concurrent atomistic-continuum study *npj Comput. Mater.* **2** 15016
[38] Xu S, Xiong L, Chen Y and McDowell D L 2017 Comparing EAM potentials to model slip transfer of sequential mixed character dislocations across two symmetric tilt grain boundaries in Ni *JOM* **69** 814–21
[39] Xu S, Xiong L, Deng Q and McDowell D L 2016 Mesh refinement schemes for the concurrent atomistic-continuum method *Int. J. Solids Struct.* **90** 144–52
[40] Xiong L, Xu S, McDowell D L and Chen Y 2015 Concurrent atomistic-continuum simulations of dislocation-void interactions in fcc crystals *Int. J. Plast.* **65** 33–42
[41] Xu S, Xiong L, Chen Y and McDowell D L 2016 Edge dislocations bowing out from a row of collinear obstacles in Al *Scr. Mater.* **123** 135–9
[42] Xu S, Xiong L, Chen Y and McDowell D L 2016 An analysis of key characteristics of the Frank-Read source process in FCC metals *J. Mech. Phys. Solids* **96** 460–76
[43] Xiong L, Rigelesaiyin J, Chen X, Xu S, McDowell D L and Chen Y 2016 Coarse-grained elastodynamics of fast moving dislocations *Acta Mater.* **104** 143–55
[44] Xu S, McDowell D L and Beyerlein I J 2019 Sequential obstacle interactions with dislocations in a planar array *Acta Mater.* **174** 160–72
[45] Xu S, Xiong L, Chen Y and McDowell D L 2017 Shear stress- and line length-dependent screw dislocation cross-slip in FCC Ni *Acta Mater.* **122** 412–9
[46] Chen H, Xu S, Li W, Ji R, Phan T and Xiong L 2018 A spatial decomposition parallel algorithm for a concurrent atomistic-continuum simulator and its preliminary applications *Comput. Mater. Sci.* **144** 1–10
[47] Xu S, Xiong L, Chen Y and McDowell D L 2017 Validation of the concurrent atomistic-continuum method on screw dislocation/stacking fault interactions *Crystals* **7** 120
[48] Mishin Y, Farkas D, Mehl M J and Papaconstantopoulos D A 1999 Interatomic potentials for monoatomic metals from experimental data and *ab initio* calculations *Phys. Rev.* B **59** 3393–407
[49] Gunter D, Kaper H and Leaf G 2002 Implicit integration of the time-dependent Ginzburg-Landau equations of superconductivity *SIAM J. Sci. Comput.* **23** 1943–58
[50] Plimpton S 1995 Fast parallel algorithms for short-range molecular dynamics *J. Comput. Phys.* **117** 1–19
[51] Xu S, Payne T G, Chen H, Liu Y, Xiong L, Chen Y and McDowell D L 2018 PyCAC: the concurrent atomistic-continuum simulation environment *J. Mater. Res.* **33** 857–71
[52] Xu S 2017 PyCAC User's Manual http://pycac.org/
[53] Xu S, Latypov M I and Su Y 2018 Concurrent atomistic-continuum simulations of uniaxial compression of gold nano/submicropillars *Phil. Mag. Lett.* **98** 173–82
[54] Henager C H and Hoagland R G 2004 Dislocation core fields and forces in FCC metals *Scr. Mater.* **50** 1091–5
[55] Henager C H and Hoagland R G 2005 Dislocation and stacking fault core fields in fcc metals *Phil. Mag.* **85** 4477–508
[56] Boleininger M, Swinburne T D and Dudarev S L 2018 Atomistic-to-continuum description of edge dislocation core: unification of the Peierls-Nabarro model with linear elasticity *Phys. Rev. Mater.* **2** 083803

[57] Chen Y 2016 The origin of the distinction between microscopic formulas for stress and Cauchy stress *Europhys. Lett.* **116** 34003
[58] Rigelesaiyin J, Diaz A, Li W, Xiong L and Chen Y 2018 Asymmetry of the atomic-level stress tensor in homogeneous and inhomogeneous materials *Proc. R. Soc.* A **474** 20180155
[59] Xu S 2018 Modelling plastic deformation of nano/submicron-sized tungsten pillars under compression: a coarse-grained atomistic approach *Int. J. Multiscale Comput. Eng.* **16** 367–76